Explanation of flicker noise with the Bak-Tang-Wiesenfeld model of self-organized criticality

Alexander Shapoval ⬤*

Department of Mathematics and Computer Science of the University of Łódź, Banacha 22, Łódź 90-238, Poland

Mikhail Shnirman ⬤

Institute of Earthquake Prediction Theory and Mathematical Geophysics RAS, Profsoyuznaya 84/32, 117997 Moscow, Russia

With the original Bak-Tang-Wisenefeld (BTW) sandpile we uncover the $1/\varphi$ noise in the mechanism maintaining self-organized criticality (SOC)—the question raised together with the concept of SOC. The BTW sandpile and the phenomenon of SOC in general are built on the slow time scale at which the system is loaded and the fast time scale at which the stress is transported outward from overloaded locations. Exploring the dynamics of stress in the slow time in the BTW sandpile, we posit that it follows cycles of gradual stress accumulation that end up with an abrupt stress release and the drop of the system to subcritical state. As the system size grows, the intracycle dynamics exhibits the $1/\varphi$-like spectrum that extends boundlessly and corresponds to the stress release within the critical state.

I. INTRODUCTION

We address the problem of the $1/\varphi$-noise construction with the sandpile model of self-organized criticality (SOC). Scholars have looked for a universal mechanism that explains the appearance of the $1/\varphi^\gamma$ noise in various physical systems. The superposition of exponentially decaying pulses is characterized by a flat low-frequency content of the spectrum that turns to the $1/\varphi^2$ decay [1]. If the rates of the decays are drawn from a uniform distribution over some interval of frequencies, then the spectrum of the superposition consists of three components: a constant, $1/\varphi$, and $1/\varphi^2$ at low, moderate, and high frequencies, respectively [2]. The change from $1/\varphi$ to $1/\varphi^\gamma$ in the spectrum is provided by the appropriate choice of the rate distribution. However, a single power law in the spectrum is not obtained with this method.

Bak, Tank, and Wiesenfeld (BTW) introduced a sandpile model as a mechanism generating power spectra [3]. This mechanism consists of a slow stress accumulation, its instant transport from overloaded locations called an avalanche, and a rare stress release at the system boundary. The BTW model has been notably influencing statistical physics for decades [4–9], revealing SOC: the critical state is attained without parameter tuning and characterized by power laws in signals themselves rather than in their spectrum [10]. Examples of SOC are associated with numerous phenomena including extremes, earthquakes, solar flares, natural language, and neuronal networks [11–16]. Nevertheless, the relationship between SOC and the flicker noise has not been fully understood yet. Papers [17,18] established that the signal generated by the linear superposition of the avalanche sizes exhibits just the

flat and $1/\varphi^2$ spectrum parts mentioned above if the dynamics is considered at so-called fast time, at which the transport of stress occurs. Reference [19] demonstrated the appearance of the $1/\varphi^\gamma$ spectrum component where the exponent γ is located between 1 and 2 with the consequent avalanche sizes. Further studies have dealt with other time scales (considering the slow time scale at which the system is loaded or the mix of the fast and slow time scales), explored the dynamics of the stress in the system, and turned to other models of SOC [4,18,20–26]. For example, the study in Ref. [4] ends up with the $1/\varphi$ spectrum exhibited by the system stress within the slow time scale introducing a specific driven mechanism and a preferable direction of the transport. Reference [22] also investigates the stress in a SOC system and introduces a dissipative transport. This generates the $1/\varphi$ spectrum component at the moderate frequencies but ruins the criticality because of dissipation. Reference [27] proposes a general mechanism resulting in various flicker noises from an initial flicker noise obtained, e.g., with SOC models.

The purpose of this paper is to uncover that the depart from the BTW-like sandpiles in the search for the $1/\varphi$ noise was premature. Revisiting the BTW model, we focus on the dynamics of stress in the system in the slow time, in contrast to the sequence of avalanche sizes, and reveal its $1/\varphi$ spectrum.

II. METHODS

A. Model

We consider the BTW model on the $N \times N$ lattice $A = \{(i, j)\}_{i,j=1}^N$ following the original formulation [3]. Integers z_{ij} interpreted as the system stress are set to the correspondence to cells $(i, j) \in A$. The cells (i, j) with $z_{ij} \geqslant 4$ are called unstable. At the initial time moment $t = t_0$, all z_{ij}

_____

*Contact author: abshapoval@gmail.com

are set to 0. Three following rules define the transition of stress $\{z_{ij}(t)\} \longrightarrow \{z_{ij}(t+1)\}$ accumulated by the beginning of time moments t and $t+1$.

(i) Graduate constant loading: A cell $(i, j) \in A$ is chosen at random and the corresponding integer is increased by one: $z_{ij}(t) = z_{ij} \longrightarrow z_{ij} + 1$.

(ii) Instant transport of stress: If the updated value of z_{ij} is less than 4, nothing more occurs at this time moment. Otherwise, let $\mathcal{N}(i, j) = \{(i \pm 1, j), (i, j \pm 1)\}$ be the set of four neighbors of the inner cell (i, j). Then the unstable cell $(i, j) \in A$ loses 4 units of stress $z_{ij} \longrightarrow z_{ij} - 4$, but each neighbor gets 1: $z_{i'j'} \longrightarrow z_{i'j'} + 1 \, \forall \, (i'j') \in \mathcal{N}(i, j)$. This transport of stress can generate other unstable cells and the same rule is applied to them.

(iii) Stress-release at a boundary cell (i, j): The set $\mathcal{N}(i, j)$ of neighbors consists of less than 4 elements. Then (ii) reads that the lattice stress is decreased by 4 but then increased only by the number of neighbors, which is 3 (or 2), so that the stress dissipates at the boundary.

The absence of unstable cells at t indicates the beginning of the time moment $t + 1$ with the obtained set $\{z_{ij}\}$ assigned to $\{z_{ij}(t+1)\}$. The transport of stress defined by (ii) and (iii) is called an avalanche. Its size is the number of the usage of rules (ii) and (iii) within the time moment. The dissipation at the boundary provides that the avalanches are finite [7]. The gradual loading, instant transport of stress, and boundary stress release constitute a general mechanism of self-organized criticality. After transient time the system attains a critical state where the avalanches exhibit a truncated power-law probability distribution of sizes with the tail exhibiting multifractal properties with respect to the lattice linear scale [28].

B. Spectrum of the mean stress

a. General idea. We examine the dynamics of the mean stress $\rho(t)$ accumulated by the lattice at the beginning of each time moment t dealing with up to 10^9 added units of stress. Our main claim presented within the results section is that the spectrum of the mean stress contains the $1/\varphi$ component and this component constitutes the essential feature of self-organized criticality. The result is justified with the spectrum binned over the intervals that are uniform in the logarithmic scale. The current section explains the necessity of such binning, initially focusing on the visualization of the spectrum as it is and the computation of the ensemble average, which produces less-dispersed spectrum curves.

b. Spectrum as it is. We start recording the catalog of the mean stress $\rho(t) = N^{-2} \sum_{i,j=1}^{N} z_{ij}(t)$ as soon as it is stabilized. The stabilization is around the value $\bar{\rho} = \lim_{\theta \to \infty} \theta^{-1} \sum_{t=\theta}^{2\theta} \rho(t)$. Zero on the time axis is assigned to the moment of the first catalog record. The dynamics of $\rho(t)$ on the interval is studied through the computation of the spectrum $S(\varphi; \rho)$ defined at frequencies $\varphi = 0, 1, 2, \dots$. A shorter notation, $S(\rho)$, is usually used. To speed up the computation we thin out the signal $\rho(t)$ narrowing the domain to each $\nu = 25$th point: $0, 25, 50, \dots$ denoting $\rho'(t)$ the thinned out function (verifying that the conclusions are stable with respect to the perturbations of ν). The spectra $S(\rho)$ and $S(\rho')$ follow each other everywhere except high frequencies corresponding to periods that are at most hundreds. However,
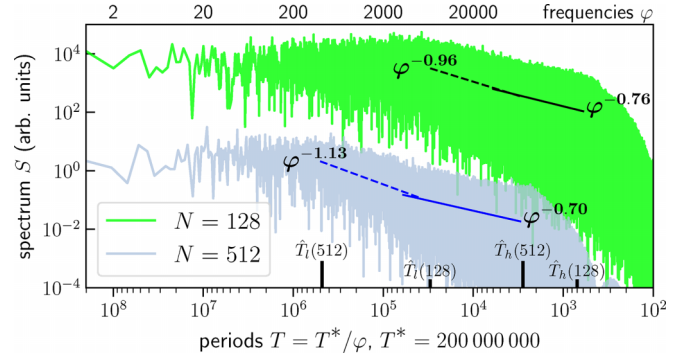

FIG. 1. Spectrum $S(\rho')$ computed with $\bar{\rho}$ defined on $[0, T^*]$, where $T^* = 2 \times 10^8$, for 128×128 and 512×512 lattices; highest frequencies are omitted. The blue and black lines give the best fits. The power laws of the type $S \sim \varphi^{-\gamma}$ imply the dependence $S \sim T^{\gamma}$.

the high-frequency content is well defined by earlier works. Therefore, the usage of the spectrum $S(\rho')$ instead of $S(\rho)$ affects the part of the frequencies that is unimportant for this study.

We display the spectrum $S(\rho')$ obtained with 128×128 and 512×512 lattices (Fig. 1). The inspection of both graphs (in green and light blue) signals that the spectrum consists of at least three parts: a quasiconstant low-frequency part, a power-law decay at moderate frequencies, and a high-frequency content decaying faster; $\hat{T}_l$ and $\hat{T}_h$ denote the visual estimates of the corresponding transition points T_l and T_h. The best fits (the dashed and solid black and blue lines in Fig. 1) computed within $[\hat{T}_h, \hat{T}_l]$ are sensitive to the interval of computation; we note the drop in the exponent from 0.96 to 0.76 and from 1.13 to 0.70 found with $N = 128$ and 512, respectively. The fits are written with *frequencies*, whereas we discuss the corresponding *periods*; the transformation of the fits $T^{\gamma} \to \varphi^{-\gamma}$ is evident.

c. Ensemble average. The uncertainty in the high- and moderate-frequency contents of the spectrum is potentially reduced through the ensemble average. Namely, the domain $[0, T]$ of any initial signal, $\{\rho(t)\}$ or $\{\rho'(t)\}$ in our case, is split into n successive parts; each of them extends to $T^* = T/n$ time moments. The spectrum of each part is computed and the average of the obtained spectra is found. The result is denoted by $S_n(\rho)$ or $S_n(\rho')$, respectively. The ensemble average for $N = 256$ and $N = 1024$ performed with $\rho(t)$, $t \in [0, 2 \times 10^7]$, is displayed by the yellow and green graphs in Fig. 2(a). With $n = 100$, we substantially reduce the uncertainty in the spectrum (with respect to Fig. 1). At the right, these graphs agree with the $\sim 1/\varphi^2$ curves served as illustrations, not fits. The $1/\varphi$ graph represented by the black dashed line in Fig. 2(a) highlights the convexity of the spectrum part located to the left of the $1/\varphi^2$ law (already noticed with Fig. 1).

Note, just-discussed yellow and green graphs in Fig. 2(a) are obtained with the relatively short catalog of $\rho(t)$ with $t \in [0, 2 \times 10^7]$, and no thinning are applied to. We have a longer catalog of $\rho(t)$ obtained when simulating 8×10^8 subsequent acts of the stress adding with $N = 1024$. Speeding up the computation, we find the spectrum with $\rho'(t)$ instead remaining with accurate values of moderate frequencies [the
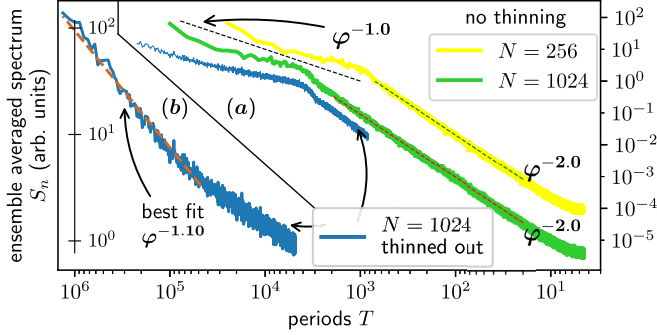
FIG. 2. Ensemble-averaged spectrum. Right part labeled (a) contains: (i) yellow and green curves $S_n(\rho)$ computed with the initial catalog $\rho(t)$, $t \in [0, 2 \times 10^7]$ split into $n = 100$ segments of the length of $T^* = 2 \times 10^5$ each for N equaled to 256 and 1024, respectively; (ii) blue curve $S_n(\rho')$ computed with the thinned catalog $\rho'(t)$, $t \in [0, 8 \times 10^8]$, $T^* = 8 \times 10^6$, $n = 100$, $N = 1024$ (the latter as for the green curve). Left part (b) sharing the horizontal axis with (a) and having the *stretched* vertical axis displays same blue curve but shown on partly different interval.

blue curve in Fig. 2(a) represents the part of the spectrum computed with ρ', $T^* = 8 \times 10^6$, $n = 100$, and $N = 1024$]. The spectra $S_n(\rho)$ and $S_n(\rho')$, the green and blue curves, respectively, are similar on the periods from $[10^3, 10^4]$ as expected. We cannot compare these graphs at larger periods (i.e., lower frequencies) because only a few points of $S_n(\rho)$ are available there.

The ensemble average allows one to partly explore the spectrum at moderate frequencies. We zoom in the vertical axis in Fig. 2(a) and redisplay the blue curve focusing on moderate frequencies located to the left of the $1/\varphi^2$ content in Fig. 2(b). Part (b) of the figure is located to the left of the part (a) sharing the same horizontal axis. The displayed curve consists of two parts, both of which admit rather an accurate linear approximation in the double logarithmic scale. We've verified (not supporting the claim by graphs) that this pattern of two quasilinear parts is stable but the exponent of the left fit, 1.12 in Fig. 2(b), is not. We recall that system stress exhibits a quasicycle dynamics, where properties of each quasicycle are related to the drop in the level of stress release caused by a characteristic avalanche starting the quasicycle. This may explain the instability of the exponent γ at the time scales covered by our catalog. A significant extension of the catalog is required to get the reliable value of γ, which is unlikely to achieve with modern computer power.

Note that our choice $n = 100$ balances two potential drawbacks. A decrease in n reduces the accuracy of each spectrum point, whereas an increase constrains the extension of the spectrum toward low frequencies [the time coordinate of the leftmost points in Fig. 2(b) is too small], which becomes the issue for large lattices.

d. Logarithmic binning. The logarithmic binning of the spectrum is used in the paper to describe the shape of the moderate spectrum more accurately. This procedure, averaging the spectrum and, thus, stabilizing each reported value, preserves the power laws and more precisely describes the quasilinear pattern highlighted above. In more detail, put $S^*(\varphi; \rho', \tau) = \sum_{\varphi' \in [\varphi/\tau, \varphi\tau]} S(\varphi'; \rho')/(\varphi(\tau - 1/\tau))$, where $\tau > 1$, and reduce
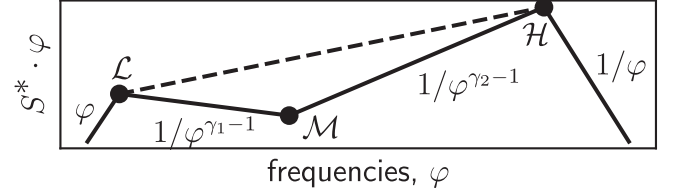

FIG. 3. Scheme of the spectrum: four components shown with solid lines.

notation to $S^*(\rho')$ when possible. One may argue that the logarithmic binning is inspired by the very nature of the definition of the spectrum because the logarithmic binning contributes to the equal representation of the periods in the spectrum points, equidistant on the logarithmic axis. Focusing on the spectrum component that is close to $1/\varphi$, we display $S^*\varphi$ instead of S^* to simplify the visual consideration of the explored spectrum part (because then the comparison with a constant is required to verify that $S^* \sim 1/\varphi$).

We have already (Figs. 1 and 2) observed four spectrum components resembling power laws. They are the high-frequency $1/\varphi^2$ part, the moderate-frequency content consisting of two parts $1/\varphi^{\gamma_1}$ and $1/\varphi^{\gamma_2}$ with $\gamma_2 < \gamma_1 < 2$, where the exponent γ_1 corresponds to lower frequencies than γ_2, and the low-frequency content represented by an approximately constant spectrum. In the $(\varphi, S^* \cdot \varphi)$ coordinate system, the exponents are increased by 1, and the spectrum components can be roughly represented by the scheme displayed in Fig. 3.

Here $\mathcal{H}$ and $\mathcal{L}$ denote the transition points from high- to moderate-frequency contents and from moderate- to low-frequency contents whereas $\mathcal{M}$ corresponds to the transition between two parts of the moderate-frequency spectrum. Our technical problem is that the segment $\mathcal{LM}$ is badly estimated numerically. However, we are able to derive the scaling of the periods T_l, T_m, and T_h, which correspond to the points $\mathcal{L}$, $\mathcal{M}$, and $\mathcal{H}$, respectively, with respect to the lattice length N. Finally, the scaling exponents and the slopes of the triangle's sides are tied through a single equation (see Appendix A) that unifies regularities derived with specific values of N.

III. RESULTS

A. Power-law spectrum components

Two power laws at moderate frequencies are displayed with $S^*\varphi$, the binned spectrum S^* multiplied by φ, in Fig. 4. Let us first comment the borders $\mathcal{L}$, $\mathcal{M}$, and $\mathcal{H}$ of the spectrum parts announced by Fig. 3, specifying the corresponding periods T_l, T_m, and T_h. We conjecture a linear relationship $T_h \sim N$ and find its agreement with the data. The transition within the moderate spectrum occurs at the point $\mathcal{M}$ with $T_m \sim N^{\sigma_\mathcal{M}}$, where the scaling exponent $\sigma_\mathcal{M}$ is separated from 1 and 2. We estimate $\sigma_\mathcal{M} \in [1.2, 1.4]$ and fix $\sigma_\mathcal{M} = 1.3$, avoiding attempts to uncover a more precise value. The points $\mathcal{L}_\infty$ in Fig. 4 marked as proxies to the left border $\mathcal{L}$ of the moderate frequency content satisfy a natural conjecture $T_l \sim N^2$, hardly verifiable by a brute force with current computer capacities.

The slopes $\Gamma_{\mathcal{MH}}$ of the fit to the spectrum over the periods $[T_h, T_m]$ are stable with respect to the parameters of the
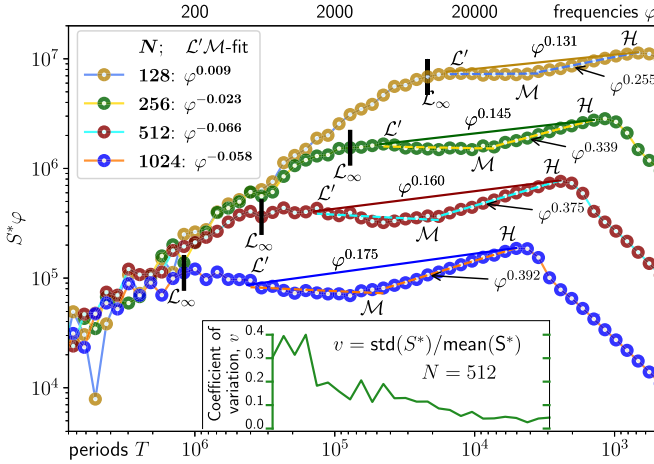
FIG. 4. Normalized spectrum $S^* \cdot \varphi$ in circles, found with logarithmic bins of the length $\tau = \sqrt{1.2}$ for four lattices. The triangles $\mathcal{L}_\infty \mathcal{MH}$ corresponds to the triangles $\mathcal{LMH}$ displayed on Fig. 3. The fits φ^Γ are found for $\mathcal{MH}$ and $\mathcal{L'M}$ instead of $\mathcal{L}_\infty \mathcal{M}$. The periods corresponding to the points $\mathcal{L}_\infty$, $\mathcal{L'}$, $\mathcal{M}$, and $\mathcal{H}$ scale as $\sim N^2$, $\sim N^{1.5}$, $\sim N^{1.3}$, and $\sim N^1$, respectively. Inset, shared period axis: the coefficient of variation of the values of the spectrum S^* related to $N = 512$.

computation. In Fig. 4, they are 0.255, 0.339, 0.375, 0.392 when N varies from 128 to 1024. These slopes saturate to a limit as N increases. We locate this limit to the interval [0.40, 0.50], but the estimate of the exact value is outside the scope of the study.

In contrast, the fit over the periods $[T_m, T_l]$ corresponding to the segment $\mathcal{ML}_\infty$ is unstable. The accuracy of the spectrum values drops with the growth in the periods T as shown with the coefficient of variation v of the spectrum values in the inset of Fig. 4. To display the inset, we split the full catalog found with the 512×512 lattice and defined on $[0, 2 \times 10^8]$ into 16 subcatalogs, compute S^* for each, and report v as the ratio of the standard deviation of these S^* to the mean. Overcoming the problem with the inaccuracy of the points in the right neighborhood of $\mathcal{L}_\infty$ we find the fits with the points $\mathcal{L'}$ that are located between $\mathcal{L}_\infty$ and $\mathcal{M}$. We assert that each point $\mathcal{L'} \in [\mathcal{M}, \mathcal{L}_\infty]$ admits its own scaling $N^{\sigma_{\mathcal{L'}}}$, where $\sigma_{\mathcal{L'}}$ varies from $\sigma_\mathcal{M}$ to 2 while $\mathcal{L'}$ moves along $[\mathcal{M}, \mathcal{L}_\infty]$. The variety of scaling exponents may be related to the multifractality of the tail of avalanches' size-frequency relationship revealed in Ref. [28]. The values of the $\mathcal{L'M}$ fit, written in the legend and considered as a proxy for the $\mathcal{L}_\infty \mathcal{M}$ fit, signal that the spectrum part which they represent are close to $1/\varphi$.

Note that if the vertices of the triangle $\mathcal{L'MH}$ do satisfy scaling relationships then the exponents $\sigma_\mathcal{H}$, $\sigma_\mathcal{M}$, and $\sigma_{\mathcal{L'}}$ and the slopes $\Gamma_{\mathcal{L'M}}$, $\Gamma_{\mathcal{MH}}$, and $\Gamma_{\mathcal{HL'}}$ are constrained by the equation

$$(\sigma_{\mathcal{L'}} - \sigma_\mathcal{M})\Gamma_{\mathcal{L'M}} + (\sigma_\mathcal{M} - \sigma_\mathcal{H})\Gamma_{\mathcal{MH}}$$
$$+ (\sigma_\mathcal{H} - \sigma_{\mathcal{L'}})\Gamma_{\mathcal{HL'}} = O(1/\log N),$$

where O in the right-hand side is the standard O-big notation and the proof is relegated to Appendix A. We check the constrain in support of the above conjecture, obtaining

that the left-hand side attains the values 0.017, 0.024, 0.019, 0.022 when N varies from 128 to 1024. These values are not dispersed and located in a proximity of 0 supporting our estimates of the $\mathcal{L}_\infty \mathcal{M}$ and $\mathcal{MH}$ spectrum parts.

Thus, we formulate our main result arguing that *the moderate spectrum* associated with the parts $\mathcal{L}_\infty \mathcal{M}$ and $\mathcal{MH}$ on Fig. 4 and located between a constant at low frequencies and the high-frequency $1/\varphi^2$ component exhibits a *complex pattern*, which is close to two power laws such that the power law at lower frequencies is approximately $1/\varphi$. The numerical analysis is stable with respect to the parameters of the computation (see additionally Appendix B).

B. Power spectrum with exponential pulses

The spectrum pattern further referred to as the 0-γ-2 pattern after the values of the exponents and consisting of a constant at low frequencies, $1/\varphi^2$ at high frequencies, and the power-law decay $1/\varphi^\gamma$ with $\gamma \approx 1$ between them can be generated by the following simple mechanism [10]. Let

$$\sum_k R(t; t_k), \quad R(t; t_k) = e^{-\lambda_k \max\{t - t_k, 0\}}, \quad (1)$$

be the sum of relaxation processes, where the decay rates λ_k are drawn from a uniform distribution over some $[\lambda_*, \lambda^*]$. Then the spectrum of the superposition exhibits the desired 0-1-2 pattern. In more detail, the Fourier transform and the spectrum of $\sum_k R(t; t_k)e^{-i\varphi t}$, $R(t; t_k) = e^{-\lambda \max\{t - t_k, 0\}}$, is, see Ref. [10],

$$\mathcal{F}(\varphi) = \int_{-\infty}^{+\infty} \sum_k R(t; t_k)e^{-i\varphi t}\, dt = \frac{1}{\lambda + i\varphi} \sum_k e^{-i\varphi t_k}$$

$$S(\varphi) = \lim_{T \to +\infty} \frac{1}{T}\langle |\mathcal{F}(\varphi)|^2 \rangle = \frac{r}{\lambda^2 + \varphi^2},$$

where r is the average pulse rate and the triangle brackets denote an ensemble average. If the process is given by the superposition of the relaxation processes, where the decay rates are drawn from a uniform distribution over some $[\lambda_1, \lambda_2]$ then the integration of the above spectrum results in the equation

$$S(\varphi) = \frac{r}{\varphi(\lambda_2 - \lambda_1)}\left(\arctan\frac{\lambda_2}{\varphi} - \arctan\frac{\lambda_1}{\varphi}\right). \quad (2)$$

Equation (2) describes the 0-γ-2 spectrum pattern with the intermediate power-law decay with the exponent $\gamma = 1$ since $S(\varphi) \approx r\pi/(2\varphi(\lambda_2 - \lambda_1))$ as $\lambda_1 \ll \varphi \ll \lambda_2$.

We argue that the sum of exponential decays corresponds to the stress accumulation $\bar{\rho} - \sum_k R(t; t_k)$ toward a mean level $\bar{\rho}$ triggered at different lattice parts in the BTW model. Indeed, let $\bar{\rho}$ be the catalog average of $\rho(t)$, and $\lambda(\rho_*)$ be the mean of the linear trend slopes derived from μ subsequent values of $\rho(t)$ following the cross of the level ρ_* in any direction. According to Fig. 5, the rate of the stress deficit λ, associated with $\frac{d}{dt}(\bar{\rho} - \sum_k R(t; t_k))$, is proportional to the stress deficit $\bar{\rho} - \sum_k R(t; t_k)$ itself, thus in line with the exponents in Eq. (1). The rates λ are from some interval $[\lambda_*, \lambda^*]$ as in Eq. (1), and the range $\lambda^* - \lambda_*$ widens as the stress approaches the critical level. Smaller slopes observed with
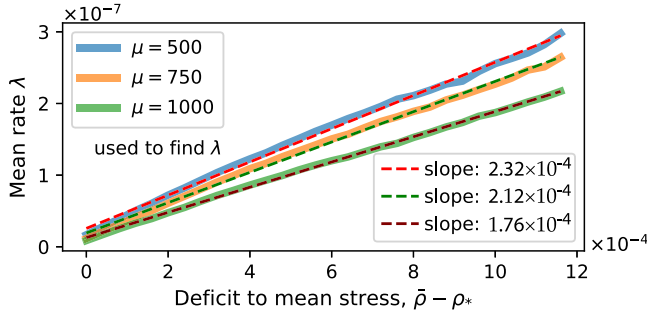
FIG. 5. Mean rate of the stress accumulation computed as the ensemble average of the slopes of the $\rho(t)$ trends that lasts μ time moments after the stress level ρ_* is passed; $N = 1024$.

larger values of μ indicate that the stress deficit is washed out more slowly with time and, consequently, with the level of stress itself, again in line with Eq. (1). Clearly, Eq. (1) only mimics the dynamics of the mean stress in the BTW sandpile. The acts of dissipation correspond to pulses, but the sign is different, as the dissipation causes the fall in stress. When the system restores after an act of dissipation, the stress grows, gradually corresponding to the decay in model Eq. (1). The BTW sandpile as well as Eq. (1) exhibit the $1/\varphi$ spectrum fragment and this property is in favor of the analogy between two models.

IV. DISCUSSION

We have exposed the details of the 0-1-2 spectrum pattern with the constant $1/\varphi$, and $1/\varphi^2$ components at low, moderate, and high frequencies respectively—exhibited by the dynamics of stress $\rho(t)$ in the BTW model. Earlier observations regarding the constant spectrum turning to the $1/\varphi^2$ decay *without* an intermediate component between them in SOC models are made with the avalanche size [18] or specific examples of non-BTW SOC models [29]. Studies [4,30] uncovered the $1/\varphi$ spectrum component in the dynamics of the stress $\rho(t)$ in a directed version of the BTW model. The 0-1-2 power-law spectrum or its modification can be obtained with the super-position of exponential pulses. This explanation agrees with our case since the stress accumulation rates depend linearly on the stress deficit (Fig. 5).

We note that the existence of the 0-1-2 pattern in a subsequent new model hardly impresses physicists. Our main contribution is that the dynamics of the system stress is characterized just by the $1/\varphi$ component if the system size is large enough. Developing the earlier paper [31] that portrayed a transition between the constant and $1/\varphi^2$ components with a specific small $N \times N$ lattice, we give the full description of this transition and highlight its value as the basic spectrum component.

In more details, the constant spectrum of the stress dynamics at the lowest frequencies (Fig. 1) is provided by the largest avalanches which are located at the right end of the size-frequency relationship and associated with an enormous dissipation. They occur when the system becomes overloaded and attains the supercritical state. The stress release makes the system drop to the subcritical state. The occurrence of

such drops divides the dynamics onto "cycles" of a different duration with the general growth of stress. Because of the different duration, the notion of quasicycles could be used instead. Just these largest avalanches are predictable in advance based on preceding patterns, which definitely occur within a single cycle [32,33]. The information about the scaling of the cycle length $T_h \sim N^2$ derived here would potentially improve the prediction.

To the right of the constant component, the spectrum follows the $1/\varphi$-like pattern (Fig. 4). This is the main spectrum component as portraying the model dynamics at the time scales that are shorter than a single cycle. We relate the underlying avalanches to the tail of the size-frequency relationship. These avalanches regulate the critical state, triggering a large stress release that balances the steady graduate stress accumulation. The $1/\varphi$ part extends to the right to such frequencies that the corresponding border is scaled as N^γ with $\gamma < 2$. As the typical scaling of the time axis is N^2, the other spectrum parts, which are located at the right, could be called insignificant.

It may happen that this insignificant spectrum part is related to the avalanches that form the power-law fragment of the size-frequency relationship just because the latter consists of only this fragment and the fast decay. If so, sequential nondissipative avalanches, which belong to the power-law segment, exhibit specific patterns in time, caught by the spectrum. The role of the $1/\varphi^\gamma$ component revealed in this study with $0 < \gamma < 1$ in the formation of these patterns is yet to be understood. The links between temporal patterns formed by avalanches and the size-frequency relationship are worth exploring with slow time (as in this study), fast time (associated with the parallel updates as in the first model [3]), and their mix [4,34–37] in order to better understand the phenomenon of SOC and improve the prediction of large avalanches.

From the very introduction of the sandpile models, researchers relate them to seismic processes [12,38]. The slow and fast time scales in the models recall, respectively, the graduate accumulation of stress by the faults and the fast stress release during earthquakes. Associating the earthquakes
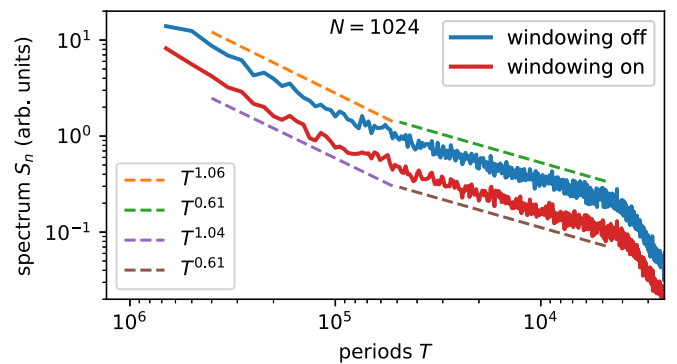

FIG. 6. Taken from Fig. 2 ensemble-spectrum average S_n (in blue) computed with $N = 1024$ and the thinned out catalog is complemented by two linear fits on the displayed intervals, the graph of another S_n computation (in red) from the same catalog ρ' but preceded by the multiplication by the Hamming window, and two fits of the latter S_n.
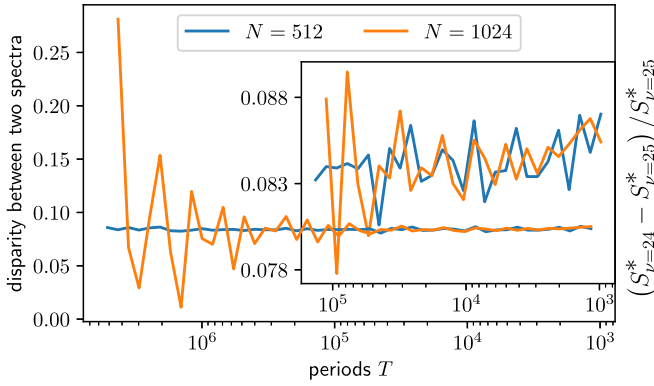
FIG. 7. The normalized difference $(S^*_{\nu=24} - S^*_{\nu=25})/S^*_{\nu=25}$ between two summed spectra S^* computed with $\nu = 24$ and $\nu = 25$ for $N = 512$ and $N = 1024$, where $S^*_{\nu=25}$ is taken from Fig. 4. Inset contains the right part of the main figure zoomed along the vertical axis.

with model avalanches, authors typically end up with unpredictability of earthquakes because of the self-similarity of the magnitude-frequency relationship [39]. Nevertheless, both seismicity and sandpiles admit a certain predictability [33,40–42]. An efficient prediction in sandpiles is performed for those large rare avalanches that are located to the right of the power-law segment of the size-frequency relationship. The knowledge about the $1/\varphi$ spectrum, which is likely related to somewhat smaller avalanches, would potentially allow to predict them. To what extent the progress in the prediction of sandpiles is movable to the theory of seismic activity is worth independent studies.

Summarizing, the dynamics of stress in the BTW sandpile is described with "cycles" of gradual stress accumulation that end up with an abrupt stress release and the drop of the system to the subcritical state. The intracycle dynamics exhibits the $1/\varphi$ spectrum that corresponds to the stress release within the critical state. The interval with this component widens toward infinity as the lattice enlarges. Thus, the critical state can be explicitly self-organized with a process characterized by the $1/\varphi$ spectrum as Bak, Tang, and Wiesenfeld may have expected introducing the phenomenon.

ACKNOWLEDGMENTS

APPENDIX A: LINEAR ALGEBRA WITH THE TRIANGLE $\mathcal{LMH}$

Dealing with the triangle $\mathcal{LMH}$ with the coordinate axis denoted by x and y as in the school handbooks, we are going to prove that $(\sigma_{\mathcal{L}} - \sigma_{\mathcal{M}})\Gamma_{\mathcal{LM}} + (\sigma_{\mathcal{M}} - \sigma_{\mathcal{H}})\Gamma_{\mathcal{MH}} + (\sigma_{\mathcal{H}} - \sigma_{\mathcal{L}})\Gamma_{\mathcal{HL}} = O(1/\log N)$, where $x_Z \sim \sigma_Z \log(N)$, $Z \in \{\mathcal{L}, \mathcal{M}, \mathcal{H}\}$, and $\Gamma_{\mathcal{LM}}$, $\Gamma_{\mathcal{MH}}$, and $\Gamma_{\mathcal{HL}}$ are the slopes of the corresponding sides. Initially, we write the definition of the slope of each side of the triangle:

$$\Gamma_{\mathcal{LM}} = \frac{y_{\mathcal{M}} - y_{\mathcal{L}}}{x_{\mathcal{M}} - x_{\mathcal{L}}}, \quad \Gamma_{\mathcal{MH}} = \frac{y_{\mathcal{H}} - y_{\mathcal{M}}}{x_{\mathcal{H}} - x_{\mathcal{M}}}, \quad \Gamma_{\mathcal{HL}} = \frac{y_{\mathcal{L}} - y_{\mathcal{H}}}{x_{\mathcal{L}} - x_{\mathcal{H}}}.$$

Multiplying each equation by the denominator and summing the equations, we find that

$$\Gamma_{\mathcal{LM}}(x_{\mathcal{M}} - x_{\mathcal{L}}) + \Gamma_{\mathcal{MH}}(x_{\mathcal{H}} - x_{\mathcal{M}}) + \Gamma_{\mathcal{HL}}(x_{\mathcal{L}} - x_{\mathcal{H}}) = 0.$$

The substitution $x_Z \sim \sigma_Z \log(N)$, $Z \in \{\mathcal{L}, \mathcal{M}, \mathcal{H}\}$, finalizes the proof.

APPENDIX B: STABILITY ISSUES

We have performed an extensive stability check of the results against the perturbation of the parameters providing here a few examples. The similarity of the spectra computed with the full catalog and the thinned out one are observed (Fig. 2) at moderate frequencies, where both spectra are accurately defined.

The computation of the spectrum as it is defined above suffers from the nonperiodicity of the signal. This affects only high-frequency content. We illustrate the reliability of the spectrum S_n at moderate frequencies repeating the computation of the spectrum but applying the Hamming window introduced in Ref. [43]. Namely, the signal is multiplied by an appropriate sine wave to equalize the ends of the signal and only then the spectrum is computed. Figure 6 exhibits a good agreement between the spectra computed in both ways. The corresponding best fits found on the displayed intervals are also in a good agreement.

Figure 7 confirms that the choice of a specific distance between the values of the initial catalog when ρ' is constructed via thinning does not affect our conclusions. We changed $\nu = 25$ to $\nu = 24$, thus taking each 24th point into consideration. The change creates generally the multiplication factor, as the normalized difference $(S^*_{\nu=24} - S^*_{\nu=25})/S^*_{\nu=25}$ between two summed spectra S^* computed with $\nu = 24$ and $\nu = 25$ slightly oscillates around a horizontal line at the frequencies of interest.

[1] W. Schottky, Small-shot effect and Flicker effect, Phys. Rev. **28**, 74 (1926).

[2] J. Bernamont, Fluctuations de potentiel aux bornes d'un conducteur metallique de faible volume parcouru par un courant, Ann. Phys. **11**, 71 (1937).

[3] P. Bak, C. Tang, and K. Wiesenfeld, Self-organized criticality: an explanation of *I/f* noise, Phys. Rev. Lett. **59**, 381 (1987).

[4] H. J. Jensen, *Self-Organized Criticality: Emergent Complex Behavior in Physical and Biological Systems* (Cambridge University Press, United Kingdom, USA, Australia, 1998), Vol. 10.

[5] G. Pruessner, *Self-Organised Criticality: Theory, Models and Characterisation* (Cambridge University Press, United Kingdom, USA, Australia, 2012).

[6] R. Dickman, A. Vespignani, and S. Zapperi, Self-organized criticality as an absorbing-state phase transition, Phys. Rev. E **57**, 5095 (1998).

[7] D. Dhar, Theoretical studies of self-organized criticality, Physica A **369**, 29 (2006).

[8] N. Watkins, G. Pruessner, S. Chapman, N. Crosby, and H. Jensen, 25 years of self-organized criticality: Concepts and controversies, Space Sci. Rev. **198**, 3 (2016).

[9] G. Mikaberidze and R. M. D'Souza, Sandpile cascades on oscillator networks: The BTW model meets Kuramoto, Chaos **32**, 053121 (2022).

[10] E. Milotti, 1/f noise: a pedagogical review, arXiv:physics/0204033.

[11] A. Levina, J. M. Herrmann, and T. Geisel, Dynamical synapses causing self-organized criticality in neural networks, Nat. Phys. **3**, 857 (2007).

[12] K. Ito and M. Matsuzaki, Earthquakes as self-organized critical phenomena, J. Geophys. Res. **95**, 6853 (1990).

[13] D. Millman, S. Mihalas, A. Kirkwood, and E. Niebur, Self-organized criticality occurs in non-conservative neuronal networks during "up" states, Nat. Phys. **6**, 801 (2010).

[14] R. T. J. McAteer, M. J. Aschwanden, M. Dimitropoulou, M. K. Georgoulis, G. Pruessner, L. Morales, J. Ireland, and V. Abramenko, 25 years of self-organized criticality: Numerical detection methods, Space Sci. Rev. **198**, 217 (2016).

[15] V. A. Gromov and A. M. Migrina, A language as a self-organized critical system, Complexity **2017**, 1 (2017).

[16] B. Tadić and R. Melnik, Self-organised critical dynamics as a key to fundamental features of complexity in physical, biological, and social networks, Dynamics **1**, 181 (2021).

[17] H. J. Jensen, K. Christensen, and H. C. Fogedby, 1/f noise, distribution of lifetimes, and a pile of sand, Phys. Rev. B **40**, 7425 (1989).

[18] J. Kertész and L. Kiss, The noise spectrum in the model of self-organised criticality, J. Phys. A **23**, L433 (1990).

[19] L. Laurson, M. J. Alava, and S. Zapperi, Power spectra of self-organized critical sandpiles, J. Stat. Mech.: Theory Exp. (2005) L11001.

[20] K. Christensen, Z. Olami, and P. Bak, Deterministic 1/f noise in nonconserative models of self-organized criticality, Phys. Rev. Lett. **68**, 2417 (1992).

[21] S. Maslov, C. Tang, and Y.-C. Zhang, *1/f* noise in Bak-Tang-Wiesenfeld models on narrow stripes, Phys. Rev. Lett. **83**, 2449 (1999).

[22] P. De Los Rios and Y.-C. Zhang, Universal 1/f noise from dissipative self-organized criticality models, Phys. Rev. Lett. **82**, 472 (1999).

[23] J. Davidsen and H. G. Schuster, 1/f α noise from self-organized critical models with uniform driving, Phys. Rev. E **62**, 6111 (2000).

[24] V. Sposini, D. S. Grebenkov, R. Metzler, G. Oshanin, and F. Seno, Universal spectral features of different classes of random-diffusivity processes, New J. Phys. **22**, 063056 (2020).

[25] P. Pradhan, Time-dependent properties of sandpiles, Front. Phys. **9**, 641233 (2021).

[26] H. J. Jensen, *Complexity Science: The Study of Emergence* (Cambridge University Press, United Kingdom, USA, Australia, 2022).

[27] A. C. Yadav, R. Ramaswamy, and D. Dhar, General mechanism for the 1/f noise, Phys. Rev. E **96**, 022215 (2017).

[28] C. Tebaldi, M. De Menech, and A. L. Stella, Multifractal scaling in the Bak-Tang-Wiesenfeld sandpile and edge events, Phys. Rev. Lett. **83**, 3952 (1999).

[29] I. Janosi and J. Kertesz, Self-organized criticality with and without conservation, Physica A **200**, 179 (1993).

[30] H. J. Jensen, 1/f noise from the linear diffusion equation, Phys. Scr. **43**, 593 (1991).

[31] A. Shapoval and M. Shnirman, Crossover phenomenon and universality: From random walk to deterministic sand-piles through random sand-piles, Int. J. Mod. Phys. C **16**, 1893 (2005).

[32] A. Shapoval and M. Shnirman, Strong events in the sand-pile model, Int. J. Mod. Phys. C **15**, 279 (2004).

[33] A. Garber, S. Hallerberg, and H. Kantz, Predicting extreme avalanches in self-organized critical sandpiles, Phys. Rev. E **80**, 026124 (2009).

[34] M. Paczuski, S. Boettcher, and M. Baiesi, Interoccurrence times in the Bak-Tang-Wiesenfeld sandpile model: A comparison with the observed statistics of solar flares, Phys. Rev. Lett. **95**, 181102 (2005).

[35] A. Deluca, N. R. Moloney, and Á. Corral, Data-driven prediction of thresholded time series of rainfall and self-organized criticality models, Phys. Rev. E **91**, 052808 (2015).

[36] A. Shapoval, B. Shapoval, and M. Shnirman, 1/x power-law in a close proximity of the Bak–Tang–Wiesenfeld sandpile, Sci. Rep. **11**, 18151 (2021).

[37] L. Baňas, B. Gess, and M. Neuß, Stochastic partial differential equations arising in self-organized criticality, arXiv:2104.13336.

[38] M. Sahimi, Earthquakes, critical phenomena, and percolation, in *Applications of Percolation Theory* (Springer, Cham, 2023), Vol. 213, pp. 101–116.

[39] R. Geller, D. Jackson, Y. Kagan, and F. Mulargia, Earthquakes cannot be predicted, Science **275**, 1616 (1997).

[40] V. Keilis-Borok, Earthquake prediction: State-of-the-art and emerging possibilities, Annu. Rev. Earth Planet Sci. **30**, 1 (2002).

[41] H. Kanamori, Earthquake prediction: An overview, in *International Handbook of Earthquake and Engineering Seismolog, Part B*, edited by W. H. K. Lee and H. Kanamori, P. C. Jennings, and C. Kisslinger, International Geophysics (Academic Press, Cambridge, Massachusetts, USA, 2003), Vol. 81, pp. 1205–1216.

[42] A. Shapoval and M. Shnirman, How size of target avalanches influences prediction efficiency, Int. J. Mod. Phys. C **17**, 1777 (2006).

[43] F. J. Harris, On the use of windows for harmonic analysis with the discrete Fourier transform, Proc. IEEE **66**, 51 (1978).